Frontiers of Physics
https://doi.org/10.1007/s11467-021-1146-x
Front. Phys.
17(2), 23502 (2022)

RESEARCH ARTICLE

Strain induced topological transitions in twisted double bilayer graphene

Guoyu Luo[1], Xinyu Lv[1], Lu Wen[1], Zhiqiang Li[1], Zhenbing Dai[2,†]

[1] *College of Physics, Sichuan University, Chengdu 610064, China*
[2] *Department of Physics, Sichuan Normal University, Chengdu 610066, China*
Corresponding author. E-mail: [†] *zhenbingdai@sicnu.edu.cn*
Received November 4, 2021; accepted January 6, 2022

We theoretically study the band structures and the valley Chern numbers of the AB–AB and AB–BA stacked twisted double bilayer graphene under heterostrain effect. In the absence of heterostrain, due to the constrains by the spatial symmetries, the central two flat bands of the AB–AB are topological trivial bands, while in the AB–BA they have a finite Chern number. The heterostrain breaks all the point group symmetries and the constrains are lifted, hence the topological properties of the two arrangements can be tuned by different strain magnitudes ε and directions φ. The heterostrain has dissimilar impacts on the Chern numbers of the AB–AB and AB–BA, owing to their different band gaps, and these gaps can be modified by a vertical electric field. Our results show that the topological transitions for both arrangements occur in the ε range of 0.1%–0.4%, which can be realized in the graphene-based sample.

Keywords valley Chern number, twisted double bilayer graphene, flat bands, heterostrain

1 Introduction

Flat bands induced by long-period moiré patterns play an important role in graphene-based moiré systems. In these flat bands with extremely narrow bandwidths, electron-electron interaction become non-negligible, resulting in a series discoveries of novel quantum phenomena such as correlated insulating states and superconductivity [1–9]. Recently, intrinsic orbital magnetism indicative of time-reversal symmetry breaking has been explored in magic angle twisted bilayer graphene (TBG) and other moiré heterostructures [9–14], which gives rise to the nontrivial topology of the flat bands. Experiments have observed quantum anomalous Hall (QAH) effect when these flat bands are partially filled [14, 15]. Moreover, the nearly flat and topological nontrivial bands are also the two essential ingredients for realize the fractional quantum Hall (FQH) effect without an external magnetic field [16–19]. A large gap between the topological nontrivial flat bands may lead to the emerging of high temperature FQH states. Therefore, engineering flat bands is of great importance.

Beside the TBG, twisted double bilayer graphene (TDBG) at certain twist angle also exhibits moiré flat bands [20–24]. The C_2 symmetry breaking in the TDBG makes its flat bands highly tunable. As a result, the topological properties and bandwidths of the flat bands can be efficiently tuned by a vertical electric field [23–26], which makes the TDBG an excellent platform to explore strongly correlated physics. Aside from the electric field, strain gives an alternative way to engineer flat bands. Strain is inevitable during the fabrication process and can be controlled by piezoelectric substrate [27]. Several results have shown that strain can heavily modify the signatures of the STM measurements or electronic transport [28–30].

In this work, we investigate the topological properties for the two arrangements of TDBG, AB–AB and AB–BA, under uniaxial heterostrain. In the absence of strain, the topological natures of the AB–AB and AB–BA are different owing to their different spatial symmetries. As the applied heterstrain breaks all the point group symmetries, the constrains on the valley Chern numbers are lifted. With the strain increases, the valley Chern numbers of the central two flat bands only depend on how the gap between them and the gaps between these bands and the adjacent bands evolve. Without a vertical electric field, the topological properties of the two flat bands can be tuned only in the AB–BA stacked TDBG, while they can be tuned in both arrangements at a certain electric field.

This work is organized as follows: we give the descriptions of the atomic structure and Brillouin zone of the TDBG in Section 2, and theoretic methods are also introduced in this section. In Section 3, we study the band structures and the topological properties of the TDBG under strain effect, where the corresponding results for both arrangements are discussed in detail. In Section 4, a brief conclusion is presented.

* Special Topic: Two-dimensional Layered Materials and Device Physics (Ed. Lei Wang). This article can also be found at http://journal.hep.com.cn/fop/EN/10.1007/s11467-021-1146-x.

2 Methods

2.1 Atomic structure and Brillouin zone

The TDBG consists of two AB-stacked bilayer graphene (BLG) rotated against each other. Here, we consider the two arrangements of TDBG, AB–AB and AB–BA, as shown in Fig. 1(a). For isolated AB-stacked BLG, there are four atoms in the unit cell labeled by A_1, B_1, A_2 and B_2. B_2 is located vertically below A_1 with strong coupling between them, which we refer to as dimer sites. For those located directly above or below the center of the hexagon, we refer to them as non-dimer sites. The lattice vectors of graphene are defined as $\boldsymbol{a}_1 = a(1,0)$ and $\boldsymbol{a}_2 = a(1/2, \sqrt{3}/2)$ and the reciprocal lattice vectors are given by $\boldsymbol{b}_1 = (2\pi/a)(1, -1/\sqrt{3})$ and $\boldsymbol{b}_2 = (2\pi/a)(0, 2/\sqrt{3})$, where $a \approx 0.246$ nm is the lattice constant of graphene. In the case of the TDBG, the first BLG is rotated by $\theta/2$ in the x–y plane and the second BLG is rotated by $-\theta/2$. Therefore, the lattice vectors of the lth BLG are written as $\boldsymbol{a}_i^{(l)} = R(\mp\theta/2)\boldsymbol{a}_i$ with $\mp$ for $l = 1, 2$ respectively, where $R(\theta)$ is the rotation matrix given by $R(\theta) = \left(\begin{smallmatrix} 1 & -\theta \\ \theta & 1 \end{smallmatrix}\right)$ for a small θ. The reciprocal lattice vectors after rotation are $\boldsymbol{b}_i^{(l)} = R(\mp\theta/2)\boldsymbol{b}_i$. Fig. 1(b) displays the Brillouin zone (BZ) of TDBG, where the large and small hexagons represent the first BZ of BLG and the first moiré BZ respectively. The reciprocal lattice vectors for the moiré patterns are given by $\boldsymbol{G}_i^{\mathrm{M}} = \boldsymbol{b}_i^{(1)} - \boldsymbol{b}_i^{(2)}$. The BLG's Dirac points are located at $\boldsymbol{K}_\xi^{(l)} = -\xi\left[2\boldsymbol{b}_1^{(l)} + \boldsymbol{b}_2^{(l)}\right]/3$,where $\xi = \pm 1$ labels the two valley of graphene. The high symmetric points of moiré BZ are marked as K_1, K_2, M_1, M_2 and Γ.

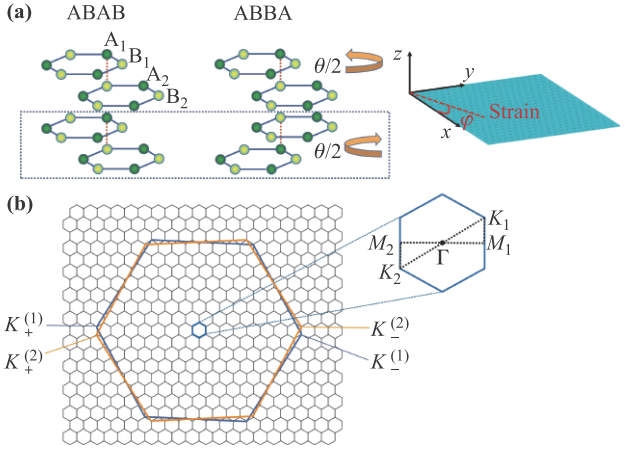

Fig. 1 **(a)** Left: Atomic structure of the AB–AB and AB–BA stacked TDBG. Right: Schematic of the strain direction. **(b)** Brillouin zone of the TDBG: the first Brillouin zones of the two graphene bilayers are represented by the two large hexagons, and the first moiré Brillouin zone is denoted by the small hexagon; black dash lines represent the momentum paths of band structure we choose in this paper.

2.2 Effective continuum model of the TDBG under strain

We use the effective continuum model to describe the low energy spectrum of the TDBG electrons under uniaxial strain [25, 26, 31, 32]. The continuum Hamiltonian of the AB–AB-stacked and AB–BA-stacked TDBG can be written as

$$H_{\mathrm{AB-AB}} = \begin{pmatrix} H_0(\boldsymbol{k}_1) & g^{\perp}(\boldsymbol{k}_1) & & \\ g(\boldsymbol{k}_1) & H_0'(\boldsymbol{k}_1) & U^{\perp} & \\ & U & H_0(\boldsymbol{k}_2) & g^{\perp}(\boldsymbol{k}_2) \\ & & g(\boldsymbol{k}_2) & H_0'(\boldsymbol{k}_2) \end{pmatrix} + \Phi,$$

$$H_{\mathrm{AB-BA}} = \begin{pmatrix} H_0(\boldsymbol{k}_1) & g^{\perp}(\boldsymbol{k}_1) & & \\ g(\boldsymbol{k}_1) & H_0'(\boldsymbol{k}_1) & U^{\perp} & \\ & U & H_0'(\boldsymbol{k}_2) & g(\boldsymbol{k}_2) \\ & & g^{\perp}(\boldsymbol{k}_2) & H_0(\boldsymbol{k}_2) \end{pmatrix} + \Phi, \tag{1}$$

where $\boldsymbol{k}_l = \boldsymbol{k} - \boldsymbol{K}_\xi^{(l)}$ with $\mp$ for $l = 1, 2$ respectively and $x^{\perp}$ represents the conjugate transpose of x. H_0 and $H_0{}'$ are the Hamiltonian of monolayer graphene in the form of

$$\begin{aligned} H_0(\boldsymbol{k}_l) &= -\sum_{\xi=\pm} \hbar v\left[(R(\theta)+S(\xi))(\boldsymbol{k}_l - \boldsymbol{D}_{l,\xi})\right]\cdot(\xi\sigma^x, \sigma^y) \\ &\quad + \begin{pmatrix} 0 & 0 \\ 0 & \Delta' \end{pmatrix}, \\ H_0'(\boldsymbol{k}_l) &= -\sum_{\xi=\pm} \hbar v\left[(R(\theta)+S(\varepsilon))(\boldsymbol{k}_l - \boldsymbol{D}_{l,\xi})\right]\cdot(\xi\sigma^x, \sigma^y) \\ &\quad + \begin{pmatrix} \Delta' & 0 \\ 0 & 0 \end{pmatrix}, \end{aligned} \tag{2}$$

where σ^x and σ^y are the Pauli matrix. Δ' represents the onsite potential difference of dimer sites with respect to non-dimer sites, and the band velocity of monolayer graphene v is taken as $\hbar v/a = 2.1354$ eV. $S(\varepsilon)$ is the uniaxial strain tensor and can be described by the strain magnitude ε and strain direction φ, which has the form [29]

$$\begin{aligned} S &= \begin{pmatrix} S_{11} & S_{12} \\ S_{21} & S_{22} \end{pmatrix} \\ &= \varepsilon \begin{pmatrix} -\cos^2\varphi + \lambda\sin^2\varphi & (1+\lambda)\cos\varphi\sin\varphi \\ (1+\lambda)\cos\varphi\sin\varphi & -\sin^2\varphi + \lambda\cos^2\varphi \end{pmatrix}, \end{aligned} \tag{3}$$

where $\lambda = 0.16$ is the Poisson ratio for graphene. In our calculation, the first and the second BLG are strained oppositely with the same magnitude of $\varepsilon/2$, which we refer to as heterostrain. Experimentally, uniaxial strain can be controlled by using flexible substrates [33] or AFM tips [34]. The strain has two impacts on the band structure of TDBG, the geometry effect of the BZ and the

shift of the original Dirac points [27]. For small strain, the shift is proportional to the strain magnitude and can be described by an effective gauge connection:

$$\boldsymbol{A} = \frac{\sqrt{3}}{2a}\beta\left(S_{11} - S_{22}, -2S_{12}\right), \tag{4}$$

where β is the hopping modulus factor determined by the type of the material. First principle calculation suggests $\beta = 3.14$ for graphene [35]. Hence, the positions of the Dirac points $\boldsymbol{D}$ are given by

$$\boldsymbol{D}_\xi = [\mathrm{II} - S(\varepsilon)]\boldsymbol{K}_\xi - \xi\boldsymbol{A}. \tag{5}$$

The interlayer coupling matrix g in AB-stacked BLG is written as

$$g(\boldsymbol{k}) = \begin{pmatrix} \hbar v_2 \boldsymbol{k}_+ & \gamma \\ \hbar v_1 \boldsymbol{k}_- & \hbar v_2 \boldsymbol{k}_+ \end{pmatrix}, \tag{6}$$

where γ is the coupling between dimer sites, and $v_1\,(v_2)$ is related to diagonal hopping with $\hbar v_1/a = 0.2771$ eV ($\hbar v_2/a = 0.0381$ eV). The matrix U represents the moiré interlayer coupling between two twisted AB-stacked BLG given by

$$\begin{aligned} U = &\begin{pmatrix} u & u' \\ u' & u \end{pmatrix} + \begin{pmatrix} u & u'\omega^{-\xi} \\ u'\omega^{\xi} & u \end{pmatrix} \mathrm{e}^{\mathrm{i}\xi \boldsymbol{G}_1^M \cdot \boldsymbol{r}} \\ &+ \begin{pmatrix} u & u'\omega^{\xi} \\ u'\omega^{-\xi} & u \end{pmatrix} \mathrm{e}^{\mathrm{i}\xi\left(\boldsymbol{G}_1^M + \boldsymbol{G}_2^M\right)\cdot \boldsymbol{r}}, \end{aligned} \tag{7}$$

where $\omega = \mathrm{e}^{2\pi\mathrm{i}/3}$, and $u = 0.0797$ eV and $u' = 0.0975$ eV are the amplitudes of interlayer coupling. The difference between u and u' is due to the relaxation effect [35].

The matrix Φ is the interlayer asymmetric potential induced by an applied vertical electric field and can be written as

$$\Phi = \begin{pmatrix} \frac{3}{2}\Delta\cdot I & & & \\ & \frac{1}{2}\Delta\cdot I & & \\ & & -\frac{1}{2}\Delta\cdot I & \\ & & & -\frac{3}{2}\Delta\cdot I \end{pmatrix}, \tag{8}$$

where I is the 2×2 unit matrix, and Δ represents the interlayer electrostatic potential difference between adjacent layers.

Previous works have discussed the influence of the small parameters v_1, v_2 and Δ' in the TDBG and twisted trilayer graphene [25, 36], thus in this work, we mainly focus on the strain effects on the topological properties of the two flat bands in the TDBG.

The Chern numbers for the nth bands can be calculated by

$$C_n = \frac{1}{2\pi}\int_{\mathrm{MBZ}} F_{n,\boldsymbol{k}}\mathrm{d}^2k, \tag{9}$$

where MBZ represents the moiré BZ, $F_{n,\boldsymbol{k}}$ is the Berry curvature defined by

$$F_{n,\boldsymbol{k}} = \frac{\partial A_{n,\boldsymbol{k}}^{(y)}}{\partial k_x} - \frac{\partial A_{n,\boldsymbol{k}}^{(x)}}{\partial k_y},$$

$$A_{n,\boldsymbol{k}}^{(\mu)} = -\mathrm{i}\left\langle u_{n,\boldsymbol{k}} \left| \frac{\partial}{\partial k_\mu} \right| u_{n,\boldsymbol{k}} \right\rangle, \tag{10}$$

where $u_{n,\boldsymbol{k}}$ is the Bloch wave function of the nth band.

The Chern number for each valley can be calculated independently as the intervalley coupling is negligible for small twist angle. Due to time reversal symmetry T, the total Chern number of the two valley must vanish. Therefore, we only show the Chern numbers of the $\boldsymbol{K}+$ valley. The space symmetry also imposes constrains on the topological properties of the TDBG. The AB–AB has a two-fold rotation symmetry C_{2x} along the x axis, while the AB–BA has a two-fold rotation symmetry C_{2y} along the y axis. The C_{2x} symmetry requires $F_{n,(\boldsymbol{k}_x,-\boldsymbol{k}_y)} = -F_{n,(\boldsymbol{k}_x,\boldsymbol{k}_y)}$, so the Chern number of each single band in the AB–AB becomes zero. The C_{2y} symmetry requires $F_{n,(\boldsymbol{k}_x,-\boldsymbol{k}_y)} = F_{n,(\boldsymbol{k}_x,\boldsymbol{k}_y)}$, meaning the Chern number can be finite in the AB–BA system.

3 Results and discussion

We calculate the band structures of TDBG with $\theta = 1.33°$, which is the angle where strong correlated states are found experimentally [3, 4, 21, 22]. Unless otherwise specified, the strain direction φ is set as 30°. As shown in Fig. 2, in the absence of heterostrain, the band structures of the AB–AB and AB–BA are quite similar, except that due to different space symmetries (C_{2x} and C_{2y}), the two flat bands are touching at two points in the AB–AB while they are separated in the AB–BA. Both arrangements exhibit electron-hole asymmetries induced by v_1, v_2 and Δ'. As discussed above, the valley Chern numbers of the two flat bands in the AB–AB must vanish while that of the upper flat band in the AB–BA is +2. In fact, as long as the gaps between the two flat bands and the adjacent bands are protected, the total valley Chern number of the two central flat bands for twisted multilayer system is determined by the stacking chiralities of the top and bottom layers, which is zero for the AB–AB and +2 for the AB–BA system [37].

The applied small heterostrain changes the geometry of the BZ and leads to differences in hopping matrix elements, which will enlarge the separation between adjacent bands and shift the locations of the Dirac point. In the TBG, the separation of the two flat bands is characterized by the separation of the corresponding van Hove singularities, which is proportional to the strain magnitude ε for small strains [27, 38]. However in TDBG, the separation of its central flat bands is dominated by the small parameters v_1, v_2 and Δ', where the small strain effect is inconspicuous. The strain induced separations can be clearly seen between the bands near the flat bands (mid and right plots in Fig. 2), and these bands become much flat when the ε increases. In the TBG, the Dirac point at each valley is protected by the combination of C_{2z} and

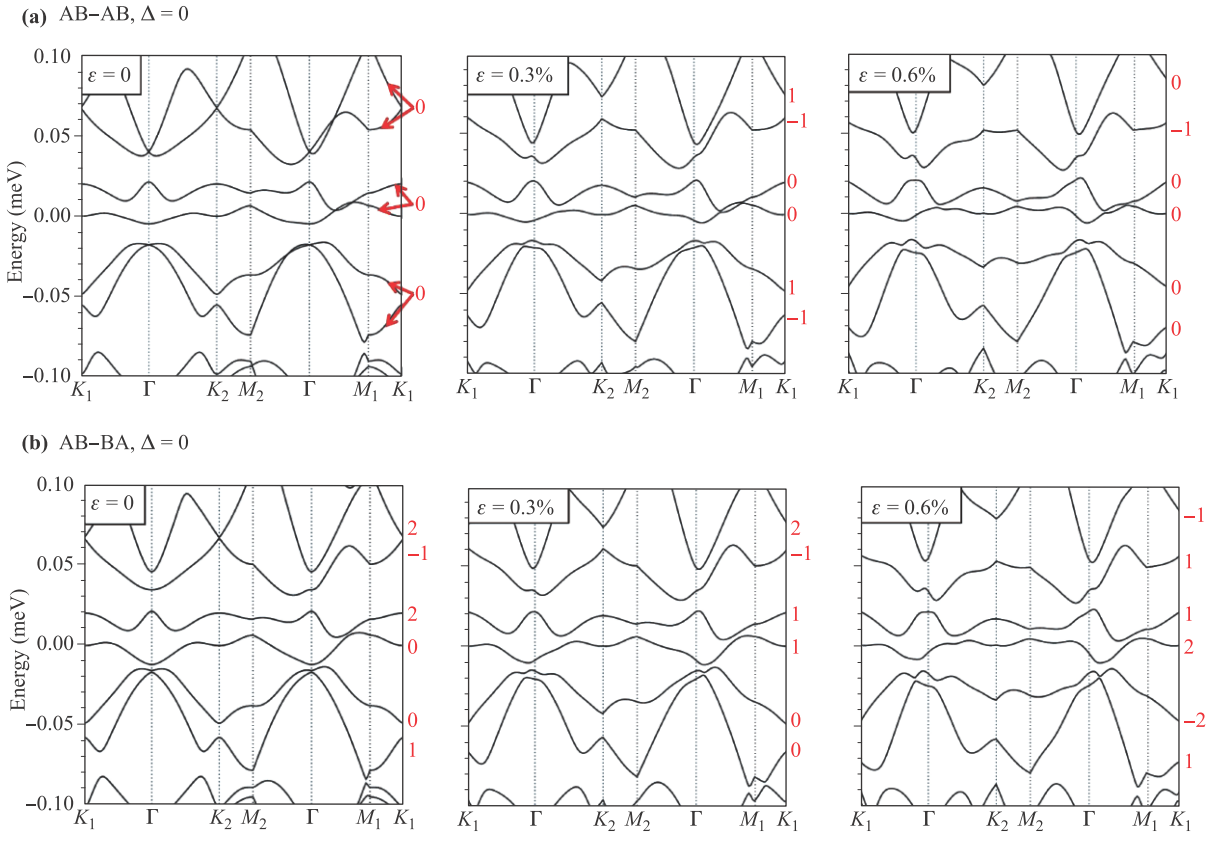

Fig. 2 **(a)** Band structures and topological properties of the AB–AB stacked TDBG with different strain magnitudes. **(b)** Corresponding plots for the AB–BA stacked TDBG. Red numbers represent the Chern numbers for the corresponding bands.

time reversal symmetry T. The strain never open a gap at Dirac point because it does not break the C_{2z} symmetry, and the locations of the low energy Dirac fermions are shifted away from the original valley. This is in sharp contrast to the TDBG, where the small parameters mentioned above have already open a gap at the Dirac point, because the TDBG is lack of C_{2z} symmetry. Note that strain will also shift the locations of the Dirac points that are already open.

The heterostrain breaks all the point group symmetry in the TDBG, which removes the constrains on the valley Chern number. For the AB–AB, the small heterostrain opens the band touching point, so the Chern number of each flat band can be well defined. Figure 2(a) shows that at different ε, the Chern numbers of the central two flat bands in AB–AB remain zero. However in the AB–BA, they can be efficiently tuned by heterostrain. Figure 2(b) show that the valley Chern numbers of the first conduction band are $+2, +1$ and $+1$ at $\varepsilon = 0, \varepsilon = 0.3\%$ and $\varepsilon = 0.6\%$, respectively. The corresponding Chern numbers of the first valence band are $0, +1$ and $+2$.

In order to explain the different behaviors of the topological properties of the two arrangements, we start to find the band touching process in the AB–BA where the Chern number of each band can be transferred. Normally, the band touching points locate at high symmetry lines. However, the heterostrain breaks all the point group symmetries which shift these points badly. To find the touching point, first we scan the different values of ε and confirm that the band touching occurs at $\varepsilon = 0.23\%$ and 0.39%. We then scan the moiré BZ by choosing different straight momentum paths at these two ε.

Figure 3 shows the band structure of the AB–BA at $\varepsilon = 0.23\%$ and 0.39% where the momentum paths are presented as the dash lines in the insets. The central two bands of AB–BA are touching with a Dirac dispersion at $\varepsilon = 0.23\%$, which transfers Chern number -1 to the first conduction band and $+1$ to the first valence band, resulting in Chern number $+1$ for both bands. As the strain increases, the central two bands are separated but the first valance band moves close to the second valence band with a touching moment at $\varepsilon = 0.39\%$. The Chern number of the first valence band increases $+1$ when the touching point gapped out. However, in AB–AB, the band gap between the two valence bands or the two conduction bands is large enough, so the central two bands keeps separated when the strain increases. Therefore, the Chern numbers of the central two bands in AB–AB remain zero for all small heterostrains.

Electric field is a common and efficient way to modulate

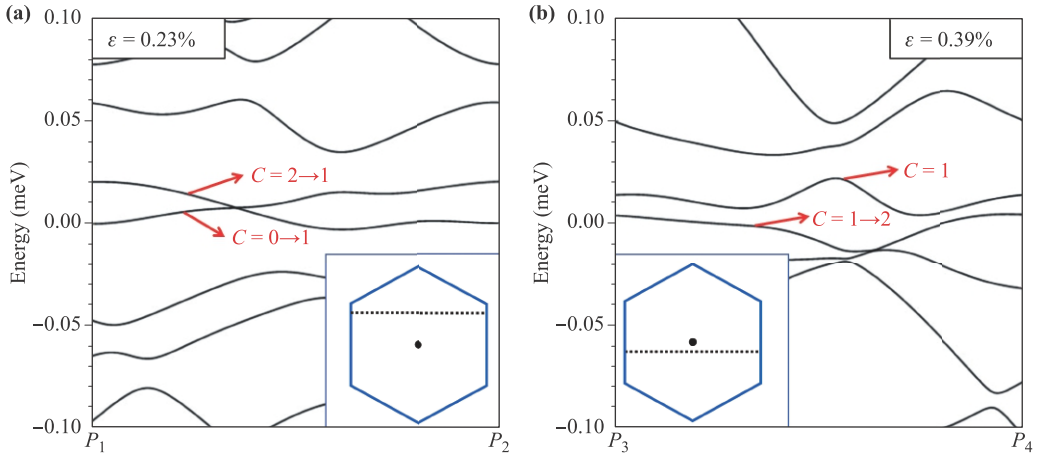

Fig. 3 Band structures of the AB–BA stacked TDBG at $\varepsilon = 0.23\%$ and 0.39%. The topological transition is accompanied by the band touching where the Chern number of each band can be transferred. The black dash lines of the insets show the momentum paths where the band touching occurs.

the electron properties of materials. The applied vertical electric field will produce different potentials in different layers, where the band gap of the material can usually be adjusted. Since the band touching process largely depends on the band gaps between adjacent layers, the topological properties under heterostrain effect at certain vertical electric field can be engrossing. Figure 4 shows the band structure of the AB–AB and AB–BA stacked TDBG with $\theta = 1.33°$ and $\Delta = 20$ meV at different ε. The electric field opens a large gap between the flat bands, which keeps the flat bands from touching. The Chern number of AB–AB can be finite because the electric field breaks the C_{2x}. For both arrangements without strain, the first conduction band is well separated from the first valence band, so the

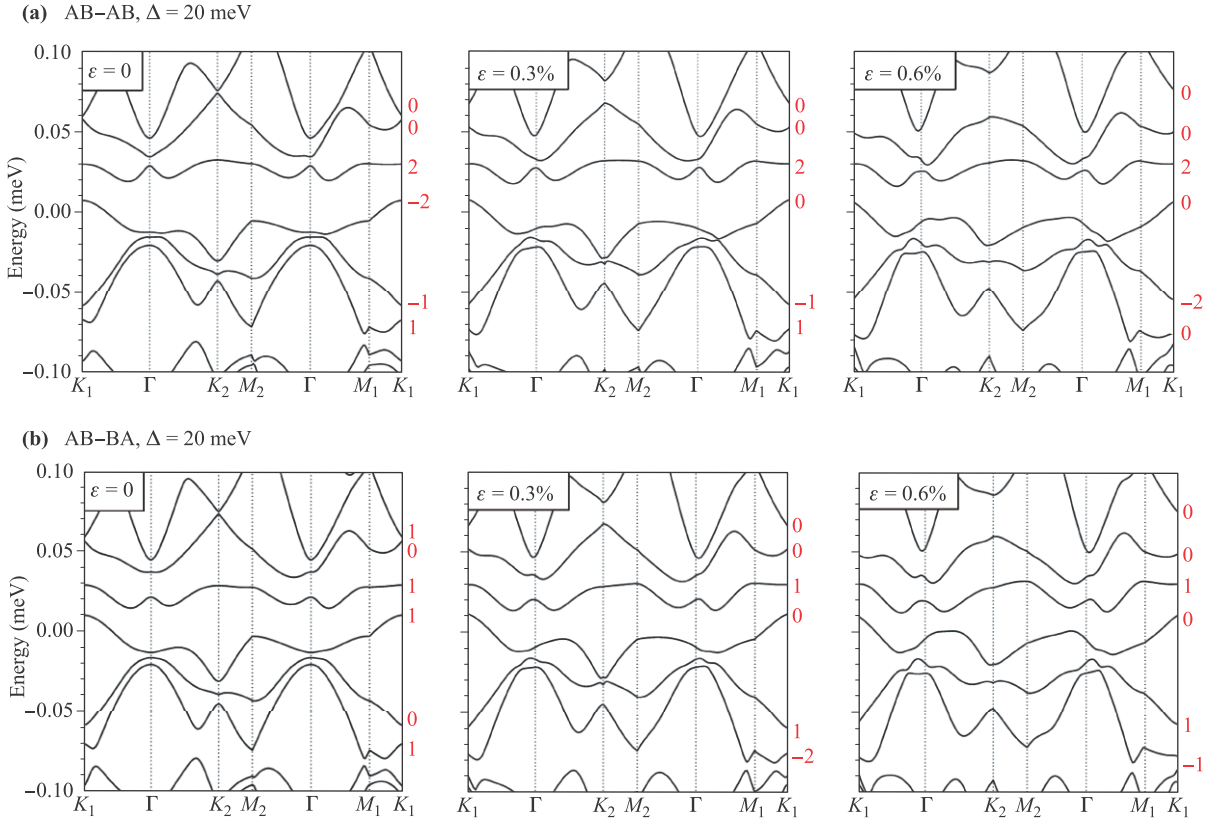

Fig. 4 **(a)** Band structures and topological properties of the AB–AB stacked TDBG at different strain magnitudes with $\Delta = 20$ meV. **(b)** Corresponding plots for the AB–BA.

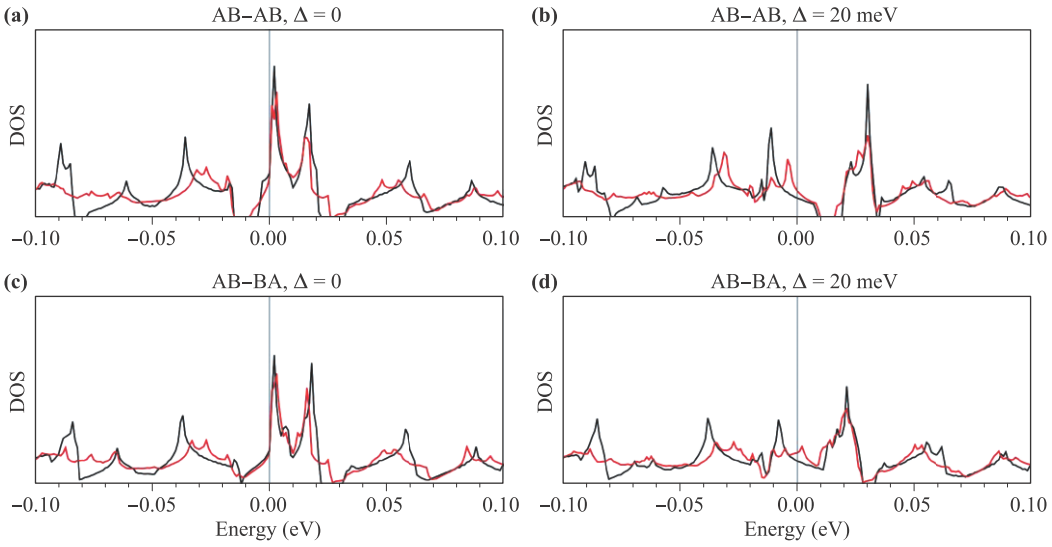

Fig. 5 **(a)** and **(b)**, Density of states of the AB–AB with $\Delta = 0$ and $\Delta = 20$ meV, respectively. **(c)** and **(d)**, corresponding plots for the AB–BA. The unstrained and strained ($\varepsilon = 6\%$) cases are plotted with black and red curves, respectively.

small heterostrain will induce no band touching for these two bands, and the Chern number of the first conduction band remains unchanged (+2). However, the applied electric field makes the first valance band much wider and the gap between the first two valance bands disappear, resulting in band touching points at small heterostrain. Therefore, the Chern number of the first valence band for both systems can be tuned by the heterostrain. We plot

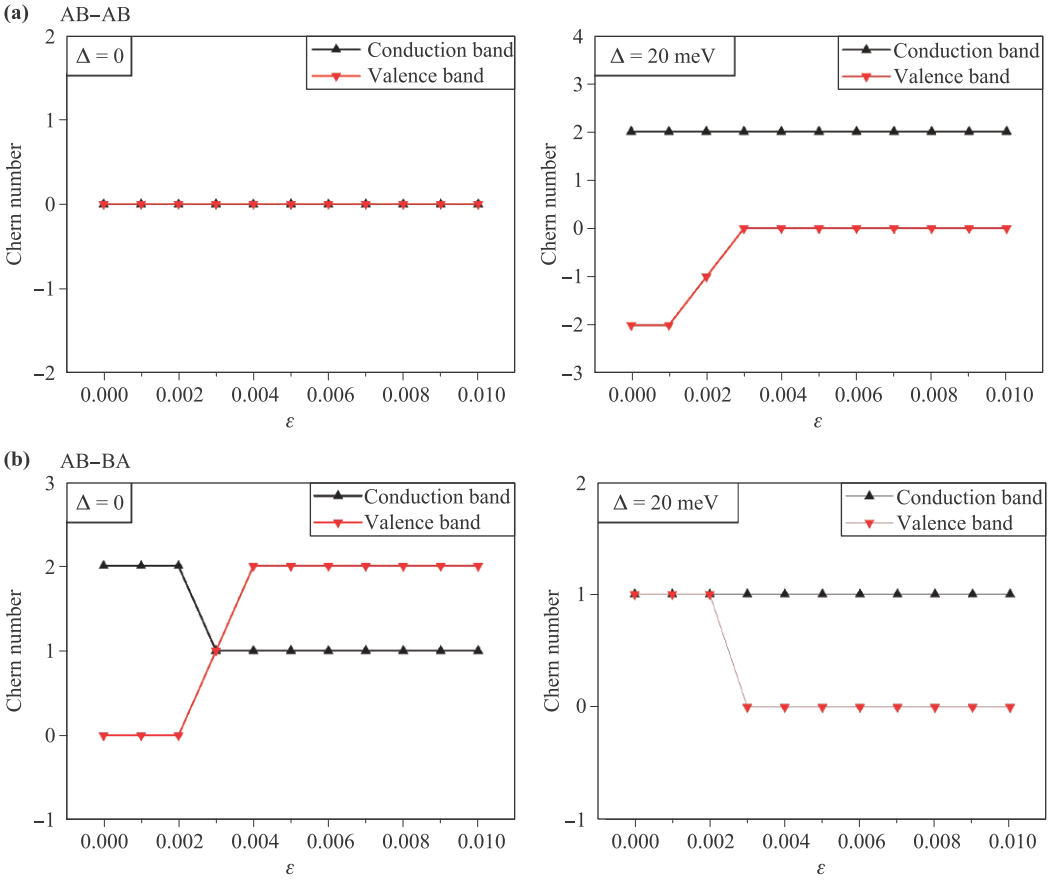

Fig. 6 **(a)** Chern numbers of the central two bands for the AB–AB stacked TDBG at different strain magnitude with $\Delta = 0$ and $\Delta = 20$ meV. **(b)** Corresponding plots for the AB–BA stacked TDBG.

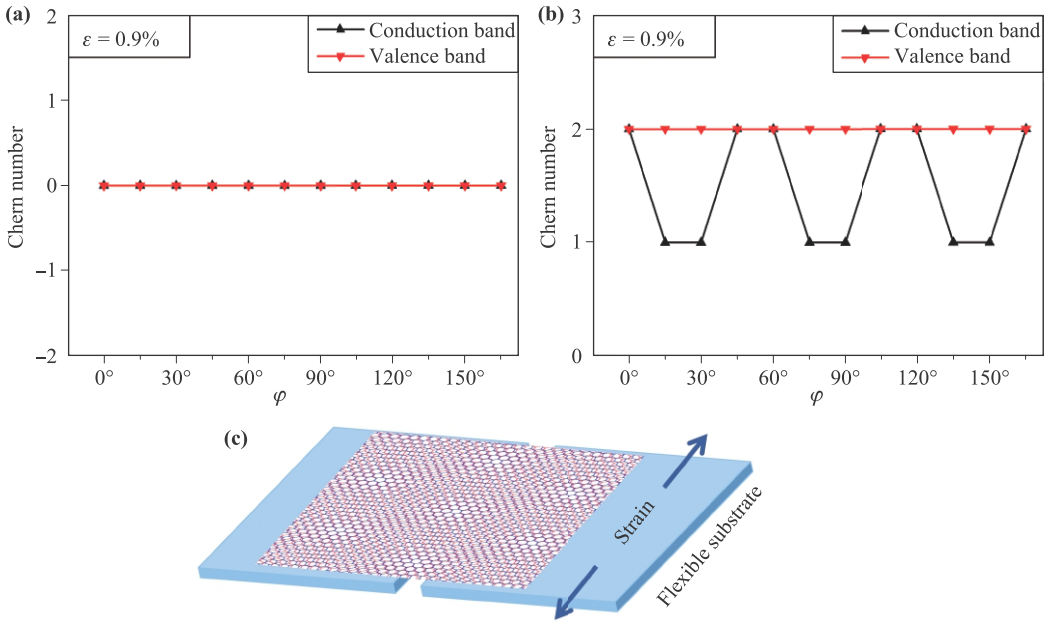

Fig. 7 **(a)** Chern numbers of the central two bands for the AB–AB stacked TDBG at different strain directions with $\Delta = 0$ and $\varepsilon = 0.9\%$. **(b)** Corresponding plots for the AB–BA stacked TDBG. **(c)** Schematic of the sample device to reveal the topological transitions under strain, the flexible substrate is used to apply uniaxial strain to the TDBG.

the density of states (DOS) for strained (red curve) and unstrained (black curve) cases of both arrangements with $\Delta = 0$ and $\Delta = 20$ meV in Fig. 5, which can clearly show how the energy gaps evolve with strain and electric field, consisting with the discussion above. The van Hove singularities of the flat bands can be slightly shifted by the applied 0.6% strain. However, the electric potential of 20 meV inhibits the van Hove singularities of the flat bands severely, especially for the lower flat band.

Figure 6 summarizes the Chern numbers of central two bands for varies of ε with different Δ. For AB–AB stacked TDBG with $\Delta = 0$, the Chern numbers of the central two bands are zero and their trivial topology can not be changed by strain, but with $\Delta = 20$ meV, the Chern number of the lower band can be tuned from -2 to 0 by different ε. As for the AB–BA with $\Delta = 0$, the topology of both bands are tunable, while with $\Delta = 20$ meV, only the Chern number of the lower band can be controlled by ε. These behaviors are depending on the details of the band structures, especially the band gaps of the involved bands. For both systems, the topological phase transition occurs in the region of ε ranging from 0.1% to 0.4%, which is a common strain range that can be realized in the graphene-based sample. As the band gaps between two central bands and the adjacent bands for the two system are of different sizes, their topological properties also behave differently on strain direction φ. Our calculations show that the Chern numbers in AB–AB are independent with φ when $\varepsilon \leq 1\%$ and $\Delta = 0$, while in AB–BA, they are sensitive to φ when $\varepsilon \geq 0.9\%$ and $\Delta = 0$. Therefore, we plot the φ dependence of the Chern number for the central two bands with $\varepsilon = 0.9\%$ and $\Delta = 0$ in Figs. 7(a) and (b). It shows that the topological properties of AB–BA can be modulated periodically from +1 to +2 by the strain directions, note that $\varphi = 0$ and 180° are physically equivalent. The homostrain effect (the two BLG are strained the same way) is also considered but not shown in this paper, as it causes no change in the topological properties of TDBG.

We give an experimental proposal that may reveal the topological transitions under strain. As shown in Fig. 7(c), a TDBG sample is transferred on the middle of two flexible substrates such as polyethylene terephthalate (PET) films. The uniaxial heterostrain can be realized by stretching the PET film in one direction. One side of the sample is strained to induce a different valley Chern number than the other side. Thus, topological edge states may emerge in the domain region between the strained and unstrained areas of the TDBG. The topological edge states can be measured through transport measurements [39], scanning tunneling spectroscopy measurements, thermoelectric imaging [40], edge-current imaging and scanning near-field optical microscopy [41].

4 Conclusion

We have theoretically studied the band structures and the valley Chern numbers of the TDBG under heterostrain effect. We consider two arrangements, AB–AB and AB–BA, which are in different spatial symmetries. In the absence

of strain, the band structures of the AB–AB and AB–BA are similar, expect only the AB–AB has the band touching points between the two flat bands. The Chern numbers of the central two flat bands for both systems are constrained, where the Chern number of each single band in AB–AB must vanish and the total Chern number of AB–BA is +2. The heterostrain changes the geometry of the MBZ and induces separations between adjacent bands. It also breaks all the point group symmetries and removes the constrains on the Chern numbers, hence the topological properties of the two arrangements can be changed. Owing to their different evolution of band gaps under heterostrain, the Chern numbers of AB–AB and AB–BA can be tuned by strain in dissimilar ways. The topological transitions for both arrangements occur in the ε range of 0.1%–0.4%, and they are sensitive to φ when $\varepsilon \geq 0.9\%$ and $\Delta = 0$. Our study indicates that even small heterostrains can have great influences on the band structures and topological properties of the TDBG, and these influences depend on their stacking orders.

Acknowledgements We thank the National Natural Science Foundation of China for the support (Grant No. 11874271). All of the results can be fully reproduced using the methods described in the article.

References

1. Y. Cao, V. Fatemi, S. Fang, K. Watanabe, T. Taniguchi, E. Kaxiras, and P. Jarillo-Herrero, Unconventional superconductivity in magic-angle graphene superlattices, *Nature* 556(7699), 43 (2018)
2. Y. Cao, V. Fatemi, A. Demir, S. Fang, S. L. Tomarken, J. Y. Luo, J. D. Sanchez-Yamagishi, K. Watanabe, T. Taniguchi, E. Kaxiras, R. C. Ashoori, and P. Jarillo-Herrero, Correlated insulator behaviour at half-filling in magic-angle graphene superlattices, *Nature* 556(7699), 80 (2018)
3. X. M. Liu, Z. Hao, E. Khalaf, J. Y. Lee, Y. Ronen, H. Yoo, D. Haei Najafabadi, K. Watanabe, T. Taniguchi, A. Vishwanath, and P. Kim, Tunable spin-polarized correlated states in twisted double bilayer graphene, *Nature* 583(7815), 221 (2020)
4. C. Shen, Y. Chu, Q. Wu, N. Li, S. Wang, Y. Zhao, J. Tang, J. Liu, J. Tian, K. Watanabe, T. Taniguchi, R. Yang, Z. Y. Meng, D. Shi, O. V. Yazyev, and G. Zhang, Correlated states in twisted double bilayer graphene, *Nat. Phys.* 16(5), 520 (2020)
5. G. Chen, A. L. Sharpe, P. Gallagher, I. T. Rosen, E. J. Fox, L. Jiang, B. Lyu, H. Li, K. Watanabe, T. Taniguchi, J. Jung, Z. Shi, D. Goldhaber-Gordon, Y. Zhang, and F. Wang, Signatures of gate-tunable superconductivity in trilayer graphene moiré superlattice, *Nature* 572(7768), 215 (2019)
6. H. C. Po, L. J. Zou, A. Vishwanath, and T. Senthil, Origin of Mott insulating behavior and superconductivity in twisted bilayer graphene, *Phys. Rev. X* 8(3), 031089 (2018)
7. Y. H. Zhang, D. Mao, and T. Senthil, Twisted bilayer graphene aligned with hexagonal boron nitride: Anomalous Hall effect and a lattice model, *Phys. Rev. Res.* 1(3), 033126 (2019)
8. Y. H. Zhang, D. Mao, Y. Cao, P. Jarillo-Herrero, and T. Senthil, Nearly flat Chern bands in moiré superlattices, *Phys. Rev. B* 99(7), 075127 (2019)
9. X. Lu, P. Stepanov, W. Yang, M. Xie, M. A. Aamir, I. Das, C. Urgell, K. Watanabe, T. Taniguchi, G. Zhang, A. Bachtold, A. H. MacDonald, and D. K. Efetov, Superconductors, orbital magnets and correlated states in magic-angle bilayer graphene, *Nature* 574(7780), 653 (2019)
10. C. L. Tschirhart, M. Serlin, H. Polshyn, A. Shragai, Z. Xia, J. Zhu, Y. Zhang, K. Watanabe, T. Taniguchi, M. E. Huber, and A. F. Young, Imaging orbital ferromagnetism in a moiré Chern insulator, *Science* 372(6548), 1323 (2021)
11. H. Polshyn, J. Zhu, M. A. Kumar, Y. Zhang, F. Yang, C. L. Tschirhart, M. Serlin, K. Watanabe, T. Taniguchi, A. H. MacDonald, and A. F. Young, Electrical switching of magnetic order in an orbital Chern insulator, *Nature* 588(7836), 66 (2020)
12. G. R. Chen, A. L. Sharpe, E. J. Fox, Y. H. Zhang, S. Wang, L. Jiang, B. Lyu, H. Li, K. Watanabe, T. Taniguchi, Z. Shi, T. Senthil, D. Goldhaber-Gordon, Y. Zhang, and F. Wang, Tunable correlated Chern insulator and ferromagnetism in a moiré superlattice, *Nature* 579(7797), 56 (2020)
13. A. L. Sharpe, E. J. Fox, A. W. Barnard, J. Finney, K. Watanabe, T. Taniguchi, M. A. Kastner, and D. Goldhaber-Gordon, Emergent ferromagnetism near three-quarters filling in twisted bilayer graphene, *Science* 365(6453), 605 (2019)
14. M. Serlin, C. L. Tschirhart, H. Polshyn, Y. Zhang, J. Zhu, K. Watanabe, T. Taniguchi, L. Balents, and A. F. Young, Intrinsic quantized anomalous Hall effect in a moiré heterostructure, *Science* 367(6480), 900 (2020)
15. F. R. Geisenhof, F. Winterer, A. M. Seiler, J. Lenz, T. Xu, F. Zhang, and R. T. Weitz, Quantum anomalous Hall octet driven by orbital magnetism in bilayer graphene, *Nature* 598(7879), 53 (2021)
16. E. Tang, J. W. Mei, and X. G. Wen, High-temperature fractional quantum Hall states, *Phys. Rev. Lett.* 106(23), 236802 (2011)
17. K. Sun, Z. Gu, H. Katsura, and S. Das Sarma, Nearly flatbands with nontrivial topology, *Phys. Rev. Lett.* 106(23), 236803 (2011)
18. T. Neupert, L. Santos, C. Chamon, and C. Mudry, Fractional quantum Hall states at zero magnetic field, *Phys. Rev. Lett.* 106(23), 236804 (2011)
19. Y. F. Wang, Z. C. Gu, C. D. Gong, and D. N. Sheng, Fractional quantum Hall effect of hard-core bosons in topological flat bands, *Phys. Rev. Lett.* 107(14), 146803 (2011)
20. N. R. Chebrolu, B. L. Chittari, and J. Jung, Flat bands in twisted double bilayer graphene, *Phys. Rev. B* 99(23), 235417 (2019)
21. G. W. Burg, J. Zhu, T. Taniguchi, K. Watanabe, A. H. MacDonald, and E. Tutuc, Correlated insulating states in twisted double bilayer graphene, *Phys. Rev. Lett.* 123(19), 197702 (2019)

22. M. H. He, Y. H. Li, J. Q. Cai, Y. Liu, K. Watanabe, T. Taniguchi, X. Xu, and M. Yankowitz, Symmetry breaking in twisted double bilayer graphene, *Nat. Phys.* 17(1), 26 (2021)
23. Y. W. Choi and H. J. Choi, Intrinsic band gap and electrically tunable flat bands in twisted double bilayer graphene, *Phys. Rev. B* 100, 201402(R) (2019)
24. X. M. Liu, C. L. Chiu, J. Y. Lee, G. Farahi, K. Watanabe, T. Taniguchi, A. Vishwanath, and A. Yazdani, Spectroscopy of a tunable moiré system with a correlated and topological flat band, *Nat. Commun.* 12(1), 2732 (2021)
25. M. Koshino, Band structure and topological properties of twisted double bilayer graphene, *Phys. Rev. B* 99(23), 235406 (2019)
26. G. Y. Luo, L. Wen, X. Y. Lv, and Z. Li, Tunable optical property and flat bands in twisted double bilayer graphene, *Phys. Lett. A* 416, 127670 (2021)
27. Z. Bi, N. Yuan, and L. Fu, Designing flat band by strain, *Phys. Rev. B* 100(3), 035448 (2019)
28. L. Huder, A. Artaud, T. Le Quang, G. T. de Laissardière, A. G. M. Jansen, G. Lapertot, C. Chapelier, and V. T. Renard, Electronic spectrum of twisted graphene layers under heterostrain, *Phys. Rev. Lett.* 120(15), 156405 (2018)
29. A. Kerelsky, L. McGilly, D. M. Kennes, L. Xian, M. Yankowitz, S. Chen, K. Watanabe, T. Taniguchi, J. Hone, C. Dean, A. Rubio, and A. N. Pasupathy, Magic angle spectroscopy, arXiv: 1812.08776 (2018)
30. M. Yankowitz, S. Chen, H. Polshyn, K. Watanabe, T. Taniguchi, D. Graf, A. F. Young, and C. R. Dean, Tuning superconductivity in twisted bilayer graphene, arXiv: 1808.07865 (2018)
31. E. McCann and M. Koshino, The electronic properties of bilayer graphene, *Rep. Prog. Phys.* 76(5), 056503 (2013)
32. P. Moon and M. Koshino, Optical absorption in twisted bilayer graphene, *Phys. Rev. B* 87(20), 205404 (2013)
33. Z. H. Ni, T. Yu, Y. H. Lu, Y. Y. Wang, Y. P. Feng, and Z. X. Shen, Uniaxial strain on graphene: Raman spectroscopy study and band-gap opening, *ACS Nano* 2(11), 2301 (2008)
34. S. B. Cronin, A. K. Swan, M. S. Unlu, B. B. Goldberg, M. S. Dresselhaus, and M. Tinkham, Measuring the uniaxial strain of individual single-wall carbon nanotubes: Resonance Raman spectra of atomic-force-microscope modified single-wall nanotubes, *Phys. Rev. Lett.* 93(16), 167401 (2004)
35. N. N. T. Nam and M. Koshino, Lattice relaxation and energy band modulation in twisted bilayer graphene, *Phys. Rev. B* 96(7), 075311 (2017)
36. Z. Ma, S. Li, Y. W. Zheng, M. M. Xiao, H. Jiang, J. H. Gao, and X. C. Xie, Topological flat bands in twisted trilayer graphene, *Sci. Bull. (Beijing)* 66(1), 18 (2021)
37. J. Liu, Z. Ma, J. Gao, and X. Dai, Quantum valley hall effect, orbital magnetism, and anomalous hall effect in twisted multilayer graphene systems, *Phys. Rev. X* 9(3), 031021 (2019)
38. Z. B. Dai, Y. He, and Z. Q. Li, Effects of heterostrain and lattice relaxation on the optical conductivity of twisted bilayer graphene, *Phys. Rev. B* 104(4), 045403 (2021)
39. L. Ju, Z. W. Shi, N. Nair, Y. Lv, C. Jin, J. Jr Velasco, C. Ojeda-Aristizabal, H. A. Bechtel, M. C. Martin, A. Zettl, J. Analytis, and F. Wang, Topological valley transport at bilayer graphene domain walls, *Nature* 520(7549), 650 (2015)
40. S. Cho, S. D. Kang, W. Kim, E. S. Lee, S. J. Woo, K. J. Kong, I. Kim, H. D. Kim, T. Zhang, J. A. Stroscio, Y. H. Kim, and H. K. Lyeo, Thermoelectric imaging of structural disorder in epitaxial graphene, *Nat. Mater.* 12(10), 913 (2013)
41. S. S. Sunku, G. X. Ni, B. Y. Jiang, H. Yoo, A. Sternbach, A. S. McLeod, T. Stauber, L. Xiong, T. Taniguchi, K. Watanabe, P. Kim, M. M. Fogler, and D. N. Basov, Photonic crystals for nano-light in moiré graphene superlattices, *Science* 362(6419), 1153 (2018)